

4 Direct spectroscopic confirmation of the young embedded proto-planet WISPIT 2c

5 CHLOE LAWLOR,<sup>1,2</sup> RICHELLE VAN CAPELLEVEEN,<sup>3</sup> GUILLAUME BOURDAROT,<sup>4</sup> CHRISTIAN GINSKI,<sup>1,2</sup>  
6 MATTHEW A. KENWORTHY,<sup>3</sup> TOMAS STOLKER,<sup>3</sup> LAIRD CLOSE,<sup>5</sup> ALEXANDER J. BOHN,<sup>3</sup> FRANK EISENHAEUER,<sup>4,6</sup>  
7 PAULO GARCIA,<sup>7,8</sup> SEBASTIAN F. HÖNIG,<sup>9</sup> JENS KAMMERER,<sup>10</sup> LAURA KREIDBERG,<sup>11</sup> SYLVESTRE LACOUR,<sup>12</sup>  
8 JEAN-BAPTISTE LE BOUQUIN,<sup>13</sup> ERIC MAMAJEK,<sup>14</sup> MATHIAS NOWAK,<sup>12</sup> THIBAUT PAUMARD,<sup>12</sup> CHRISTIAN STRAUBMEIER,<sup>15</sup>  
9 NIENKE VAN DER MAREL,<sup>3</sup> AND THE EXOGRAVITY COLLABORATION

10 <sup>1</sup>*School of Natural Sciences, Center for Astronomy, University of Galway, Galway, H91 CF50, Ireland*

11 <sup>2</sup>*Ryan Institute, University of Galway, Galway, H91 TK33, Ireland*

12 <sup>3</sup>*Leiden Observatory, Leiden University, Postbus 9513, 2300 RA Leiden, The Netherlands*

13 <sup>4</sup>*Max Planck Institute for Extraterrestrial Physics, Gießenbachstraße 1, 85748 Garching, Germany*

14 <sup>5</sup>*Center for Astronomical Adaptive Optics, Department of Astronomy, University of Arizona, 933 N. Cherry Avenue, Tucson, AZ 85718, USA*

15 <sup>6</sup>*Department of Physics, Technical University of Munich, 85748 Garching, Germany*

16 <sup>7</sup>*Faculdade de Engenharia, Universidade do Porto, rua Dr. Roberto Frias, 4200-465 Porto, Portugal*

17 <sup>8</sup>*CENTRA – Centro de Astrofísica e Gravitação, IST, Universidade de Lisboa, 1049-001 Lisboa, Portugal*

18 <sup>9</sup>*School of Physics and Astronomy, University of Southampton, Southampton, SO17 1BJ, United Kingdom*

19 <sup>10</sup>*European Southern Observatory, Karl-Schwarzschild-Straße 2, 85748 Garching, Germany*

20 <sup>11</sup>*Max Planck Institute for Astronomy, Königstuhl 17, 69117 Heidelberg, Germany*

21 <sup>12</sup>*LIRA, Observatoire de Paris, Université PSL, CNRS, Sorbonne Université, Université de Paris, 5 place Jules Janssen, 92195 Meudon, France*

22 <sup>13</sup>*Univ. Grenoble Alpes, CNRS, IPAG, 38000 Grenoble, France*

23 <sup>14</sup>*Jet Propulsion Laboratory, California Institute of Technology, 4800 Oak Grove Drive, Pasadena, CA 91109, USA*

24 <sup>15</sup>*1st Institute of Physics, University of Cologne, Zùlpicher Straße 77, 50937 Cologne, Germany*

25 (Received December 15, 2025; Revised January 12, 2026; Accepted February 24, 2026)

26 Submitted to ApJ

27 ABSTRACT

28 WISPIT 2 is a nearby young star with a multi-ringed disk which was recently confirmed to host a  
29  $\sim 4.9 M_{\text{Jup}}$  gas giant planet embedded in a large (60 au) gap at a radial separation of 57 au from the  
30 host star. We confirm and characterise a **second**, close-in planet in the WISPIT 2 system using a  
31 combination of new VLT/SPHERE *H*-band dual-polarisation imaging and VLTI/GRAVITY *K*-band  
32 interferometric observations of the WISPIT 2 system.

33 The GRAVITY detection is consistent with a point-like source while its extracted *K*-band spectrum  
34 shows CO band-head absorption at 2.3  $\mu\text{m}$  and a continuum shape consistent with a young giant  
35 planet. From the GRAVITY data we extract a medium resolution *K*-band spectrum of the companion  
36 and fit **atmospheric model grids using the species tool with nested sampling to constrain**  
37 **its effective temperature, radius, and luminosity. We infer  $T_{\text{eff}}$  of 1500-2600 K, a radius**  
38 **of 0.91-2.2  $R_{\text{Jup}}$ , and a luminosity of (-3.47)-(-3.63). Comparison with evolutionary tracks**  
39 **implies a mass range of 8-12  $M_{\text{Jup}}$ , approximately twice as massive as the previously**  
40 **confirmed WISPIT 2b. The astrometry rules out a background source and marginally detects**  
41 **orbital motion of WISPIT 2c, which needs further follow-up observations for confirmation. WISPIT**  
42 **2 now becomes an analogue to PDS 70, offering a second laboratory for studying the**  
43 **formation and early evolution of a multi-planet system within its natal disk.**  
44  
45

*Keywords:* protoplanetary disks (1300) – Exoplanets(498) – Exoplanet formation(492) – Direct imaging(387) – Interferometry(808) – Spectroscopy(1558)

## 1. INTRODUCTION

The detection of thousands of extrasolar planets with indirect detection methods indicates that planet formation is an efficient process that happens commonly around young stars (see e.g. [Lissauer et al. 2023](#)). At the same time, high resolution observations of planet-forming disks at multiple wavelengths have now revealed intricate sub-structures in more than a hundred systems (see recent surveys by [Avenhaus et al. 2018](#); [Andrews et al. 2018](#); [Öberg et al. 2021](#); [Garufi et al. 2024](#); [Ginski et al. 2024](#)).

This indicates that planet-formation is indeed ongoing in many of these systems, yet the direct detection of embedded planets has proven challenging (e.g. see discussion in [Milli et al. 2012](#); [Currie et al. 2023](#)). While there are mechanisms that can shape transitional disks without requiring the presence of planets ([Marcus et al. 2015](#); [Flock et al. 2017](#); [Suriano et al. 2018](#); [Kurtovic et al. 2018](#); [Kuznetsova et al. 2022](#)), many of these systems provide strong indirect evidence for ongoing planet formation. To date there are only a few such young, disk-bearing systems in which planets or strong candidates have been confirmed, such as PDS 70 ([Keppler et al. 2018](#); [Haffert et al. 2019](#)), AB Aur ([Currie et al. 2022](#)), and HD 169142 ([Hammond et al. 2023](#)). It is the detection of these planets in formation that gives us key insights into the primary formation mechanisms that are at work in the earliest phases of system evolution, **be it through core accretion ([Pollack et al. 1996](#)) or gravitational instability ([Boss 1997](#))**.

Recently, the WISPIT 2 system has been added to the short list of confirmed planet-bearing disks ([van Capelleveen et al. 2025](#); [Close et al. 2025a](#)). Uniquely among systems with a confirmed embedded planet, the planet-forming disk in the WISPIT 2 system shows an extended multiple-ringed structure. The primary star in the system is a young solar analogue ([van Capelleveen et al. 2025](#)) of  $5.1_{-1.3}^{+2.4}$  Myrs, based on stellar isochrones, which gives the intriguing possibility to observe the earliest formation history around a system similar to our own. The embedded planet within the system is located between the innermost two rings at a semi-major axis of  $57_{-3}^{+8}$  au and is estimated to have a mass of  $4.9_{-0.6}^{+0.9}$   $M_{\text{Jup}}$  ([van Capelleveen et al. 2025](#)). The presence of up to four confirmed rings with intermediate gaps, as well as a central cavity in the system, gave rise to speculation that this could be a multi-planet system in formation, possibly comparable to PDS 70, or a younger version of

HR 8799 ([Marois et al. 2008](#)). Indeed [Close et al. \(2025a\)](#) pointed out that a signal (referred to as CC1) appears to be present in their  $L$ - and  $z'$ -band observations at a projected separation of  $\sim 15$  au within the central disk cavity. In this letter we present new observations of this companion candidate using VLT/SPHERE (Spectro-Polarimetric High-contrast Exoplanet REsearch; [Beuzit et al. 2019](#)) and VLTI/GRAVITY ([GRAVITY Collaboration et al. 2017a](#)) confirming the presence of a second planet in the WISPIT 2 system.

## 2. OBSERVATIONS

In addition to the observations presented in [van Capelleveen et al. \(2025\)](#), we obtained new high-angular resolution data with both the VLT/SPHERE Infrared Dual-band Imager and Spectrograph (IRDIS; [Dohlen et al. 2008](#)) and VLTI/GRAVITY, providing up to date  $H$ -band images and  $K$ -band interferometry observations, respectively.

### 2.1. GRAVITY Observations

The GRAVITY observations ([GRAVITY Collaboration et al. 2017b](#)) were carried out on the four Unit Telescopes (UT) on 2025-10-05. The observations were executed in Service Mode (program ID: 115.29HG.001) with good-to-average atmospheric conditions, and a spectral resolution of  $R \sim 500$ . The log of the observations is included in Table 1. The GRAVITY observations were obtained in dual-field on-axis mode. In this mode, the Fringe-Tracker (FT) fiber stabilises the fringes on the host star, and the Science Channel (SC) fiber alternates between the planet and the star ([GRAVITY Collaboration et al. 2019](#)). The pointing of the SC fiber was informed by the SPHERE  $H$ -band images and with an initial guess at  $\Delta\text{RA}, \Delta\text{Dec} = (-22.87 \text{ mas}, -107.6 \text{ mas})$  from the host star. These observations benefit from the GRAVITY+ extreme Adaptive Optics system (GPAO; [GRAVITY+ Collaboration 2025](#)) to reduce the speckle noise close-in to the host star and maximise the flux injected in the planet, using the high-order correction with the Natural Guide Star sensor ([Bourdardot et al. 2024](#)). The data were reduced using the ESO GRAVITY pipeline ([Lapeyrere et al. 2014](#)). The observations were taken together with an interferometric calibrator in order to measure normalised visibilities. We used the `exogravity` pipeline <sup>1</sup> to extract the relative astrometry

<sup>1</sup> <https://gitlab.obspm.fr/mnowak/exogravity>

Target	UT Date	Instrument	Setup	NEXP/NDIT/DIT	Airmass	$\tau_0$ (ms)	seeing (")
WISPIT 2	2025-10-05	VLTI/GRAVITY	MEDIUM	12/8/30s	1.1-1.3	3.1-5.1	0.51 - 0.79
HD 180595 (CAL)	2025-10-05	VLTI/GRAVITY	MEDIUM	1/32/3s	1.6	4.3	0.59
<b>WISPIT 2</b>	<b>2025-09-24</b>	<b>VLT/SPHERE</b>	<b>H-band</b>	<b>48/1/64s</b>	<b>1.2 <math>\pm</math> 0.1</b>	<b>5.7 <math>\pm</math> 1.2</b>	<b>0.8 <math>\pm</math> 0.2</b>

Table 1: Log of the GRAVITY and SPHERE observations.

and contrast spectrum of the companion relative to the host star. We integrate the GRAVITY spectrum over the 2MASS  $K_s$ -band filter curve to obtain the  $K_s$ -band magnitude included in Table 2.

### 2.2. SPHERE H-band observations

To extract the properties of WISPIT 2c, we use the SPHERE H-band data observed on UTC date 2025-03-21 described in van Capelleveen et al. (2025). In addition, we obtained a new SPHERE/IRDIS H-band observation carried out as part of program 115.29HG.002 (PI C. Ginski) on UTC date 2025-09-24 with a similar observation setup, see Table 1. This observation includes a dedicated reference observation obtained with the star-hopping technique, alternating approximately every 10 minutes between WISPIT 2 and a reference star. During the science sequence, we obtained 12 full polarimetric cycles, each comprising exposures at the 4 half-wave plate positions ( $Q^+$ ,  $Q^-$ ,  $U^+$ ,  $U^-$ ). Each individual exposure had an integration time of 64 seconds, resulting in a total on-target DPI exposure of 51.2 minutes. Over the full science sequence, the pupil-tracking configuration delivered a total parallactic angle rotation of 19.6 degrees. Between science cycles, we recorded 20 reference-star frames with an exposure time of 64 seconds.

In this study we focus on the total intensity reduction of the SPHERE data and only used the polarised intensity imagery to confirm that there is no strong dust scattering signal present at the position of the investigated companion. We extracted the photometry and astrometry of the companion (see Table 2) using negative planet injection combined with a simplex minimisation technique, followed by Bayesian inference using Markov chain Monte Carlo (MCMC; MacKay 2003) with 200 walkers and 10,000 steps, and repeated this method for fake positive injections at positions equidistantly distributed in polar space to extract the systematic errors of the method. All steps are executed with PynPoint modules, and the centering precision of 2.5 mas of the star behind the coronagraph, as well as uncertainties in pixel scale, true North correction, and pupil offset,

were included in the error budget, analogues to what is described in van Capelleveen et al. (2025). However, instead of Angular Differential Imaging (ADI) we used Reference Differential Imaging (RDI) with Principal Component Analysis (PCA). Given that the position of WISPIT 2c is on the inner working angle of the coronagraph, following the recommendation outlined in the SPHERE manual<sup>2</sup>, we apply a correction for the transmission profile of the coronagraph to both the science frames and the reference library. As the observation from UTC date 2025-03-21 did not have a dedicated reference observation, we leveraged the H-band RDI library described in van Capelleveen et al. (2025). For the observation of UTC date 2025-09-24 we used the dedicated reference-star observations. We found the optimal number of principal components for RDI/PCA to be 12 and 14, respectively. Due to the presence of the bright inner ring, the systematic errors of the method varied with position angle (PA). To account for this we only included systematic errors similar to those near WISPIT 2c in our error budget; between a PA of 335 degrees and 15 degrees (to the north of WISPIT 2) and between a PA of 120 and 225 degrees (to the south of WISPIT 2). The detection of WISPIT 2c after PCA/RDI in both observations is included in Fig. 1.

## 3. NATURE OF THE COMPANION

### 3.1. Re-detection of the companion with GRAVITY and SPHERE

We re-detect the planetary companion WISPIT 2c with both GRAVITY and SPHERE (see Fig. 1), providing independent confirmation of the source previously referred to as CC1 and reported by Close et al. (2025a). The detection of embedded, self-luminous protoplanets is a particularly challenging task. In the case of young planets embedded in a protoplanetary disk, it is necessary to distinguish the contribution of the scattered light of the disk from the thermal emission from the

<sup>2</sup> SPHERE manuals: <https://www.eso.org/sci/facilities/paranal/instruments/sphere/doc.html>

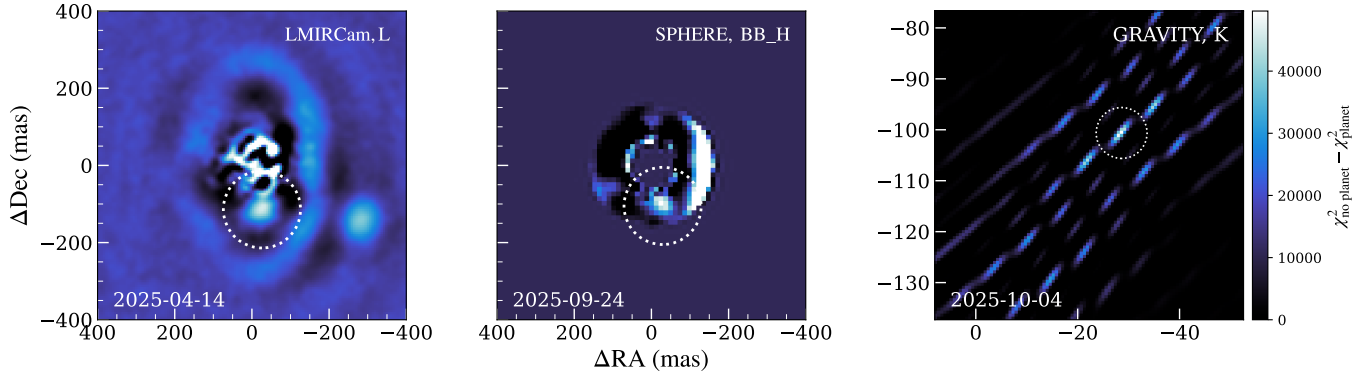


**Figure 1:** *Left panel:* Original  $L$ -band detection of CC1 in [Close et al. \(2025a\)](#). *Middle panel:* New  $H$ -band detection of WISPIT 2c following RDI. We show a confined annulus that was used for optimal stellar signal subtraction. Note that the bright arch on the right side of the annulus is the forward scattering side of the circumstellar disk. *Right panel:* Detection map of WISPIT 2c planet with VLTI/GRAVITY on the night of 2025-10-04. **The map shows the periodogram power maps of a point source companion as a function of angular offset from the star, where the companion location corresponds to the strongest peak.**

planet. Substructures in the disk are usually of comparable scales to the Point Spread Function of 10m class telescopes. Interferometry is intrinsically sensitive to the coherent emission of point-like sources, which is distinct from the extended background disk signal. The GRAVITY data are key observational evidence for the detection of a new protoplanet in this work.

We followed the approach of [GRAVITY Collaboration et al. \(2019\)](#) and [Wang et al. \(2021\)](#) to model the coherent flux of the planet  $V_{planet}(b, t, \lambda)$  measured with GRAVITY:

$$V_{planet}(b, t, \lambda) = C(\lambda)V_{star}(b, t, \lambda) \exp(i\Phi(b, t, \lambda)) \quad (1)$$

expressed as a function of  $b$  the baseline, time  $t$  and wavelength  $\lambda$ , with  $C(\lambda)$  the contrast spectrum  $C(\lambda)$  estimated from the exoGRAVITY pipeline, as described in [Nowak et al. \(2020\)](#), and  $V_{star}(\lambda) = F_{star}(\lambda)J_{star}(b, t, \lambda)$  the coherent flux of the star. The normalised visibility of the star  $J_{star}(b, t, \lambda)$  was calibrated on a reference star HD 180595. We modelled the star spectrum  $F_{star}(\lambda)$  using a BT-Settl-CIFIST stellar model ([Fig. 7](#)), as detailed in [Appendix A](#).

The phase  $\Phi(b, t, \lambda)$  of the planet signal is defined as:

$$\Phi(b, t, \lambda) = -\frac{2\pi}{\lambda}(\Delta RA.u + \Delta DEC.v) \quad (2)$$

wherein  $(u, v)$  are the coordinates in the frequency domain, and  $(\Delta RA, \Delta DEC)$  the sky-coordinates of the planet relative to the star. The detection map using this point-source model is shown in [Fig. 1](#). The detection map shows the periodogram power maps  $z(\Delta RA, \Delta DEC) = \chi_{no\ planet}^2 - \chi_{planet}^2(\Delta RA, \Delta DEC)$

over the GRAVITY fiber field-of-view, as described in [Eq. \(B.6\)](#) of [Nowak et al. \(2020\)](#). The peak of the detection indicates a point-like source, with the side lobes characteristic of the uv-coverage of the UT interferometric array. The planet is detected with a  $SNR > 10$  in each of the 12 exposures with GRAVITY. The best-fit is achieved at a location of  $\Delta RA, \Delta DEC = (-29.07 \pm 0.024 \text{ mas}, -101.35 \pm 0.038 \text{ mas})$ . The presence of a CPD in addition is discussed in [Section 4.2](#).

### 3.2. Is it a bound planet?

To ascertain the nature of the object labelled CC1 by [Close et al. \(2025a\)](#), we follow two independent lines of investigation. We first determine if, with currently available astrometry, we can rule out that the object is a distant background star and secondly we test if the GRAVITY spectrum as well as the existing photometry are consistent with an object of planetary nature.

The GRAVITY  $K$ -band observation yields a relative astrometry of  $105.44 \pm 0.04 \text{ mas}$  and  $196.00 \pm 0.01^\circ$ . However, the SPHERE  $K_s$ -band observation presented in [van Capelleveen et al. \(2025\)](#) is unusable for astrometry extraction as the source lies too close to the coronagraph, influencing both the photometry and astrometry. With no available published suppression profile of the  $K_s$ -band coronagraph, we cannot confidently extract either of these parameters. The  $L$ -band astrometry presented in [Close et al. \(2025a\)](#) is close to its resolution limit for its wavelength and therefore carries large error bars in both separation and position angle and is therefore not sufficiently constraining. At such small separations we find that even if the PSF is misaligned by 0.5 of a pixel, this would change the position angle by approximately  $2.8^\circ$ , making the measurement highly sensitive to

small systematics. Although the  $z'$ -band data by [Close et al. \(2025a\)](#) provide the longest baseline and smallest error bars, the source appears slightly extended and may include scattered light or CPD emission, which could bias the central position. **In addition to these literature values from [Close et al. \(2025a\)](#), we have extracted the astrometric position of the object from both SPHERE  $H$ -band observation epochs, i.e. the epoch taken in March of 2025 and originally published in [van Capelleveen et al. \(2025\)](#) and the new SPHERE  $H$ -band observation taken in September of 2025 and presented in this study (see Appendix B Fig. 8 for a side-by-side comparison). As we describe in section 2.2 we applied a total intensity reference differential imaging reduction to both of these data sets which recovers WISPIT 2c. Conversely to the SPHERE  $K_s$ -band epoch, a detailed coronagraphic throughput profile is available for the  $H$ -band observations in the SPHERE manual. We thus can reliably extract both astrometry and photometry of WISPIT 2c. However, because the position of WISPIT 2c lies near the 50% transmission of the coronagraph, the photometry is sensitive to the accuracy of the throughput correction. Uncertainty in the position of the star behind the coronagraph could lead to small variations in throughput correction, which has not been propagated into the photometric uncertainty of the companion. While this may result in underestimated  $H$ -band magnitude uncertainties, this effect has been partially mitigated by averaging measurements from two independent epochs using two independent reference libraries. Nevertheless, this does not address the possibility of a systematic magnitude offset resulting from over- or under-correction of the throughput if the transmission profile itself is not accurate.**

We show all astrometric measurements in Fig 2. In the same figure we also illustrated the expected location of a non-moving background source. Due to the short time base-line the relative position angle of a gravitationally bound, co-moving source and a background object show considerable overlap. However, we do expect a strong change in separation for a background object that should not be present for a co-moving source. **We find that in position angle the literature data from [Close et al. \(2025a\)](#) in combination with our new GRAVITY observation appears to rule out a background object, while the SPHERE  $H$ -band epochs are consistent with both a background object and a co-moving bound planet. In separa-**

**tion the GRAVITY and SPHERE  $H$ -band data, as well as the literature  $z'$ -band data rule out a background object, while the  $L$ -band data uncertainties are too large to distinguish between both scenarios.** Given that the data points with the smallest uncertainties appear to rule out a non-moving background object, both in position angle and separation, we conclude that WISPIT 2c is a bound object in the system.

However, we note that the object shows a measurable change in position angle and separation compared to the GRAVITY measurement. This suggests that the object exhibits genuine orbital motion. Assuming the planet lies in the disk plane (inclination fixed at  $45^\circ$ ), we estimate the possible orbital solutions with *orbitize!* ([Blunt et al. 2020](#)) using an EMCEE MCMC sampler ([Foreman-Mackey et al. 2013](#)). **Based on the current astrometry we can explain the tentative change with Keplerian orbits, albeit with some inconsistency between the SPHERE  $H$ -band and literature  $z'$  and  $L$ -band data points. While the former indicate orbital motion in the same direction as the outer planet WISPIT 2b as reported in [van Capelleveen et al. \(2025\)](#), the latter exhibit a change in position angle which would put the orbit of 2c in retrograde relative to 2b. We illustrate both prograde and retrograde solutions in our proper motion analysis in Fig 2.** We note that a retrograde orbit would be extremely unusual and given the potential biases in the  $z'$ -band centroid and the limited precision of the  $L$ -band measurement, we find the pro-grade orbit indicated by the SPHERE  $H$ -band data to be the more likely scenario. Additional high-precision astrometry will be required to confirm the orbital direction of WISPIT 2c.

**With a distant background object ruled out by the astrometric analysis we inspected the  $K$ -band spectrum of WISPIT 2c.** Fig. 3 shows CO absorption in the GRAVITY  $K$ -band spectrum at  $2.2935 \mu\text{m}$ , and a positive slope from  $2.15 - 2.25 \mu\text{m}$ , both well-established signatures of young, low-gravity substellar objects ([Patience et al. 2012](#); [Allers & Liu 2013](#)). Such CO absorption is expected to remain prominent in the atmospheres of young giant planets but is not produced at detectable levels in stellar photospheres beyond temperatures of  $\sim 5300 \text{ K}$  ([Cesetti et al. 2013](#)). The photometric measurement in the  $H$ -band may follow the characteristic triangular continuum shape which arises from deep  $\text{H}_2\text{O}$  absorption both sides of the  $1.65 \mu\text{m}$  peak ([Allers & Liu 2013](#)), though our current data cannot confirm this as we cover this wavelength regime only with a single photometric point.

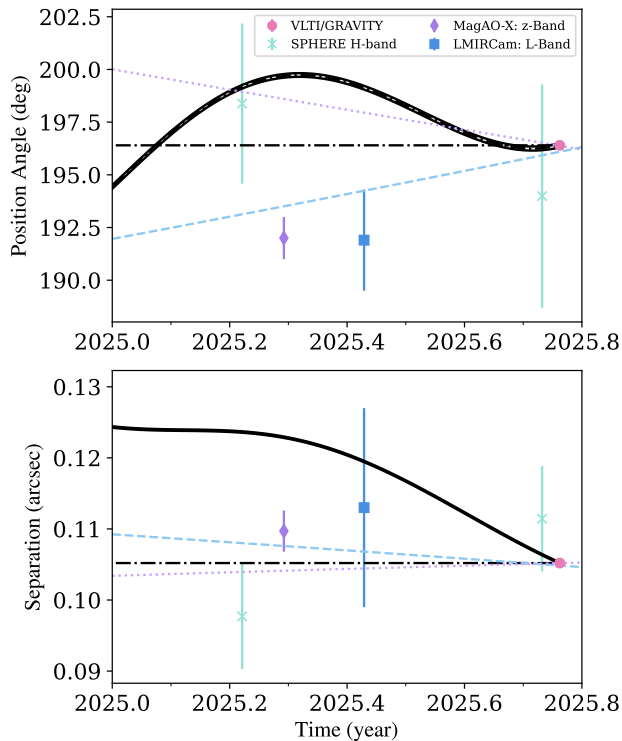


**Figure 2:** Relative astrometry of WISPIT 2c to the primary star over time. We give the separation and position angle (measured from North over east). The purple dashed-line indicates plausible orbital motion for a prograde orbit, while the blue dashed-line indicates retrograde motion. Both orbits are in the plane of the circumstellar disk. The solid “curved” line indicates the expected behaviour for a distant background object. While the black dashed-line represents no relative change of motion in relation to the host star.

Taken together, both the astrometry as well as the spectroscopic data are strongly indicating that CC1 is indeed a second planet in the system which we will now refer to as WISPIT 2c.

### 3.3. Temperature and mass of WISPIT 2c

To assess the atmospheric properties of WISPIT 2c, we employed the spectral and photometric tool species (Stolker et al. 2020b), which is commonly used for the analysis of directly imaged planets and brown dwarfs. We performed an atmospheric parameter inference by sampling self-consistent atmospheric model grids with the nested sampler dynasty (Speagle 2020) fitting the Drift-Phoenix (Hauschildt & Baron 1999; Baron et al. 2003; Voitke & Helling 2003, 2004; Helling & Voitke 2006; Helling et al. 2008a,b; Witte et al. 2009, 2011) model. We furthermore explore also sev-

eral additional models, the results of which we describe in Appendix D.

Drift-Phoenix is designed for the dust-rich atmospheres we expect of young embedded planets, and includes detailed cloud microphysics (Rajpurohit et al. 2012). For the atmosphere constraint we consider the  $z'$ - and  $L$ -band photometric points by (Close et al. 2025a) as well as our new SPHERE  $H$ -band photometric measurement and GRAVITY  $K$ -band spectrum. We discuss in Appendix D how the recovered parameters are influenced if we use various sub-sets of these data points. As we are not sensitive to variations in  $\log g$  (see Appendix D Fig. 10), varying  $\log g$  between 3 and 5 does not significantly modify the inferred atmospheric parameters. Taking an average of the available  $\log g$  values for young ( $< 50$  Myr) gas giants (Schneider et al. 2011), returns an average  $\log g$  of  $\sim 3.9$ , which we take as a fixed value. As WISPIT 2 is a solar type star we fix  $[\text{Fe}/\text{H}]$  at 0.0, similar to  $\log g$  we are not sensitive to changes in metallicity (see Appendix D Fig. 11).

Employing the Drift-Phoenix model, we derive max likelihood planet parameters of  $T_{\text{eff}} = 1754 \pm 16$  K, and  $R = 1.78 \pm 0.03 R_{\text{Jup}}$ , where the errors are purely statistical (see Appendix D, Fig. 12 for model distributions). Since the pure statistical uncertainties are clearly underestimating the possible temperature and radius range for the planet, we considered the full set of explored models in Appendix D to obtain a temperature range of 1500-2600 K, and a radius range of  $0.91$ - $2.20 R_{\text{Jup}}$ .

The distribution of temperatures appears bimodal, hence we separate the models into high and low temperature families, where more specific ranges can be seen in Table 3. We note, however, that the ranges produced by the BT-Dusty, Sonora-Bobcat, BT-Sett1, and ATMO models appear unphysical, as such a young object is expected to have an inflated radius (see for example Spiegel & Burrows 2012). Given that the Drift-Phoenix model is a closer fit to our  $K$ -band spectrum with minimal residuals and produces more reasonable temperature and radius values, we consider these values more likely. This conclusion is further strengthened by comparison of the  $K_s$ -band magnitude and  $H - K_s$  colour against evolutionary isochrones, (see discussion below), which imply inflated radii larger than  $1.6 R_{\text{Jup}}$ .

We show the best fit Drift-Phoenix model and overlay our extracted GRAVITY  $K$ -band spectrum and  $z'$ -,  $H$ -, and  $L$ -band photometry in Fig. 3. The model spectrum closely follows our

Instrument	UT Date	Band	Magnitude	Separation (mas)	PA (deg)	Ref.
MagAO-X	2025-04-16	$z'$	$19.40^{+0.65}_{-0.26}$	$109.7 \pm 2.9$	$192.0 \pm 1.0$	(Close et al. 2025a)
LBTI/LMIRcam	2025-06-05	$L$	$14.80^{+0.76}_{-0.43}$	$113.0 \pm 14.0$	$191.9 \pm 2.4$	(Close et al. 2025a)
<b>VLT/SPHERE</b>	<b>2025-03-21</b>	$H$	<b><math>16.40 \pm 0.39</math></b>	<b><math>97.69 \pm 7.42</math></b>	<b><math>198.38 \pm 3.85</math></b>	<b>This work</b>
<b>VLT/SPHERE</b>	<b>2025-09-24</b>	$H$	<b><math>16.25 \pm 0.29</math></b>	<b><math>111.45 \pm 7.39</math></b>	<b><math>193.99 \pm 5.25</math></b>	<b>This work</b>
VLTi/GRAVITY	2025-10-05	$K$	$16.04 \pm 0.01$	$105.44 \pm 0.03$	$196.00 \pm 0.02$	This work

Table 2: Apparent magnitudes and relative astrometry of WISPIT 2c.

461 extracted  $K$ -band spectrum, with a characteris- 504  
 462 tic CO absorption at  $2.2935 \mu\text{m}$  and overtones 505  
 463 between  $2.33\text{-}2.36 \mu\text{m}$ , highlighted in the inset 506  
 464 of Fig. 3. The best fit results for the alterna- 507  
 465 tive models that we explored are shown in ap- 508  
 466 pendix D (Fig. 13). The BT-Dusty, Sonora-Bobcat, 509  
 467 BT-Sett1, and ATM0 models converge toward high 510  
 468 temperature ( $\sim 2300\text{-}2600 \text{ K}$ ) solutions that im- 511  
 469 ply unphysically small radii ( $0.91 - 1.07 R_{\text{Jup}}$ ), 512  
 470 inconsistent with expectations for a young, in- 513  
 471 flated object. Given that our two best fitting 514  
 472 models, Drift-Phoenix and ExoRem, i.e. the mod- 515  
 473 els with the smallest residuals, both include 516  
 474 cloud physics, this may suggest that WISPIT 517  
 475 2c possesses a dusty atmosphere, given that the 518  
 476 planet is still young, this is expected due to its 519  
 477 low surface gravity (Marley & Sengupta 2011; 520  
 478 Charnay et al. 2018).

479 In addition to our model grid exploration, we 522  
 480 compare the GRAVITY  $K$ -band spectrum of 523  
 481 WISPIT 2c with the spectra of PDS 70b and 524  
 482 HR8799 e which are taken from the ExoGRAV- 525  
 483 ITY  $K$ -band spectral library of gas giants and 526  
 484 brown dwarfs presented in (Kammerer et al. 527  
 485 2025). These two objects were selected based on 528  
 486 their similar absolute luminosity compared to 529  
 487 WISPIT 2c. The resulting comparative spectra 530  
 488 are shown in Fig. 4. We note that the contin- 531  
 489 uum shape and depth of CO absorption features 532  
 490 of WISPIT 2c and HR8799 e are overall similar. 533  
 491 While HR8799 e is found to be slightly colder 534  
 492 than WISPIT 2c ( $1100\text{-}1400 \text{ K}$ , Nasedkin et al. 535  
 493 2024), it confirms that our spectrum is consis- 536  
 494 tent with a young gas-giant planet. Conversely 537  
 495 the spectrum of PDS 70b, a planet still located 538  
 496 within its' birth disk, appears almost flat with 539  
 497 no strong CO feature. Wang et al. (2021) discuss 540  
 498 that the spectrum is most likely explained by a 541  
 499 planetary atmosphere with significant amounts 542  
 500 of dust, the nature of which is uncertain. The 543  
 501 difference in spectrum between PDS 70b and 544  
 502 WISPIT 2c may then indicate that the former 545  
 503 is still strongly embedded, while this is not true

504 for the latter.

505 Using the luminosity derived from our radius and tem-  
 506 perature range, we estimate the mass of WISPIT 2c  
 507 by comparison to evolutionary model isochrones. To  
 508 determine the sensitivity of our mass estimate to as-  
 509 sumptions of age and evolutionary models, we computed  
 510 isochrones for WISPIT 2c using a range of represen-  
 511 tative ages and atmosphere grids. In Fig. 5, we show  
 512 isochrones at 3.8, 5.1, and 7.5 Myr (the system age  
 513 of 5.1 Myr and its associated errors reported in van  
 514 Capelleveen et al. 2025). For each age we compare the  
 515 predicted luminosity-mass relations with our measured  
 516 luminosity, including its uncertainty range, taken from  
 517 our posterior samples. Across this age span, we infer a  
 518 corresponding mass range of approximately  $8\text{-}12 M_{\text{Jup}}$ ,  
 519 consistent with the values previously reported for CC1  
 520 by Close et al. (2025a) of  $8\text{-}10 M_{\text{Jup}}$ . We tested how ro-  
 521 bust this estimate is against the usage of different model  
 522 isochrones and found a mass range of roughly  $9\text{-}11 M_{\text{Jup}}$ ,  
 523 i.e. smaller than the range given by the uncertainty of  
 524 the system age. Based on these mass ranges, it appears  
 525 likely that WISPIT 2c sits comfortably in a range of  $8\text{-}$   
 526  $12 M_{\text{Jup}}$ . However, we note that our atmospheric  
 527 grid models infer a broader range of masses of  
 528  $3\text{-}16 M_{\text{Jup}}$ . Since mass is not a fitted parameter  
 529 in these models but is instead derived from the  
 530 fixed  $\log g$  and inferred radius, we do not con-  
 531 sider these to be robust mass estimates as our  
 532 data is not sensitive to small changes in  $\log g$  as  
 533 mentioned previously.

534 In addition to our spectral analysis, the pho-  
 535 tometry of WISPIT 2c is shown in a colour-  
 536 magnitude diagram in Fig. 6, along with that  
 537 of WISPIT 2b and other known planets with  
 538 available  $H$ - and  $K_s$ -band magnitudes. Com-  
 539 parison against 5.1 Myr Sonora-Bobcat (Mar-  
 540 ley et al. 2021) and Sonora-Diamondback (Mor-  
 541 ley et al. 2024) isochrone tracks confirm that  
 542 WISPIT 2c is a planetary-mass companion, and  
 543 that the  $H - K_s$   $1\sigma$  upper bound is consistent  
 544 with a cloudy model, in agreement with the best-  
 545 fit atmosphere models to the combined spec-

trum and photometry. We note that the lower temperature and inflated radius are also preferred from comparison against these evolutionary isochrones.

Planet parameters	High T	Low T
$T_{\text{eff}}$ K	2300-2600	1500-1750
$\log g$	3.9 <sup>a</sup>	3.9
$[Fe/H]$	0.0	0.0
$R_p/R_{\text{Jup}}$	0.91-1.07	1.78-2.20
$\log L_p/L_{\odot}$	(-3.47)-(-3.53)	(-3.55)-(-3.63)
$M_p/M_{\text{Jup}}$	3-14	10-16
$M_p/M_{\text{Jup}}$		8-12 <sup>b</sup>

<sup>a</sup>Note the exception of the BT-Dusty model where  $\log g$  is 4.5.

<sup>b</sup>Mass range derived from luminosity-mass isochrones.

**Table 3: Ranges of physical parameters of WISPIT 2c based on the atmospheric model fitting from the models presented in Appendix D, were we separate based on high and low temperature families. Note: The ranges are based on the highest and lowest most likelihood values of each model, and we do not report statistical errors as they are negligible.**

## 4. DISCUSSION

### 4.1. Comparison with PDS 70

The young T Tauri star PDS 70 (Gregorio-Hetem et al. 1992) once acted as a lone candle in the dark for early planet formation studies, owing to its two confirmed planets, PDS 70b (Keppler et al. 2018) and PDS 70c (Haffert et al. 2019). The confirmation of two planets in the young WISPIT 2 system now provides a valuable second comparison point, helping to narrow the observational gap in our understanding of how giant planets convene within their natal disks. Although the sample of directly imaged, still embedded protoplanets remains too small for robust statistical analyses, it is still informative to compare the orbital architectures of WISPIT 2 and PDS 70.

PDS 70 exhibits a well-defined inner cavity, host to two planets, measuring roughly 70 au (Hashimoto et al. 2012; Dong et al. 2012; Hashimoto et al. 2015; Keppler et al. 2019) similar to that of WISPIT 2’s prominent 60 au gap, containing one planet, with a second planet sitting beyond the innermost ring. Both systems show strong signs of being shaped by their respective planets. Despite the more extended disk in WISPIT 2, the confirmed planets in both systems occupy a broadly similar radial regime, approximately 57 and 14 au for

WISPIT 2b and c, and 21 and 35 au for PDS 70b and c (Haffert et al. 2019). The lack of a dust ring between the planets in PDS 70 is likely due to the close separation between its respective planets. These planets likely would have accreted material from both sides of the ring early in their formation stages, thus depleting the dust ring and forming the large cavity that now harbours these planets. While the planets in WISPIT 2 are at a much larger separation and therefore are unable to efficiently clear the material between them, allowing the dust ring to remain intact. Recent astrometric fits by Trevascus et al. (2025) place upper mass limits of 4.9  $M_{\text{Jup}}$  and 13.6  $M_{\text{Jup}}$  for PDS 70b and c respectively, comparable to the masses of WISPIT 2b and c. These broadly similar radial and mass ranges may imply the existence of a “Goldilocks zone” for early giant planet formation, where conditions in both systems appear to be conducive to generating giant multi-planet architectures. It is likely that the planets in both WISPIT 2 and PDS 70 formed in-situ (see van Capelleveen et al. 2025; Perotti et al. 2023), implying their current locations trace the environments that supported their formation rather than the endpoints of substantial inward or outward migration.

### 4.2. Non-detection of $H\alpha$ and CPD

Despite its larger mass compared to the previously detected outer planet WISPIT 2b, there was no significant  $H\alpha$ -emission detected at the position of WISPIT 2c (Close et al. 2025a). Given that accretion generally scales with mass (see e.g. Ercolano et al. 2014; Manara et al. 2023) this indicates that either the accretion on the object is highly variable, or that the object is veiled by circumplanetary dust, which effectively blocks the optical wavelength emission. As we only have a single epoch of  $H\alpha$  imaging of the system to date, we are unable to verify if the accretion signatures of the planet might be variable. However, from large spectroscopic surveys we know this commonly to be the case for young stars (e.g. Manara et al. 2021). Given that the transport mechanisms within the disk for accretion onto the central star or a surrounding planet are similar, it is reasonable to assume that this is indeed the case also for the accretion activity of the planet. This indeed has been recently confirmed for the planets in the PDS 70 system (Close et al. 2025b; Zhou et al. 2025).

On the other hand Close et al. (2025a) point out that the  $z'$ -band measurement appears to be tentatively extended, consistent with a CPD signal within the Hill radius of a massive planet. Conversely, our preliminary GRAVITY observation rule out the presence of a compact CPD at scales of  $\sim 0.25$  au. This may indicate

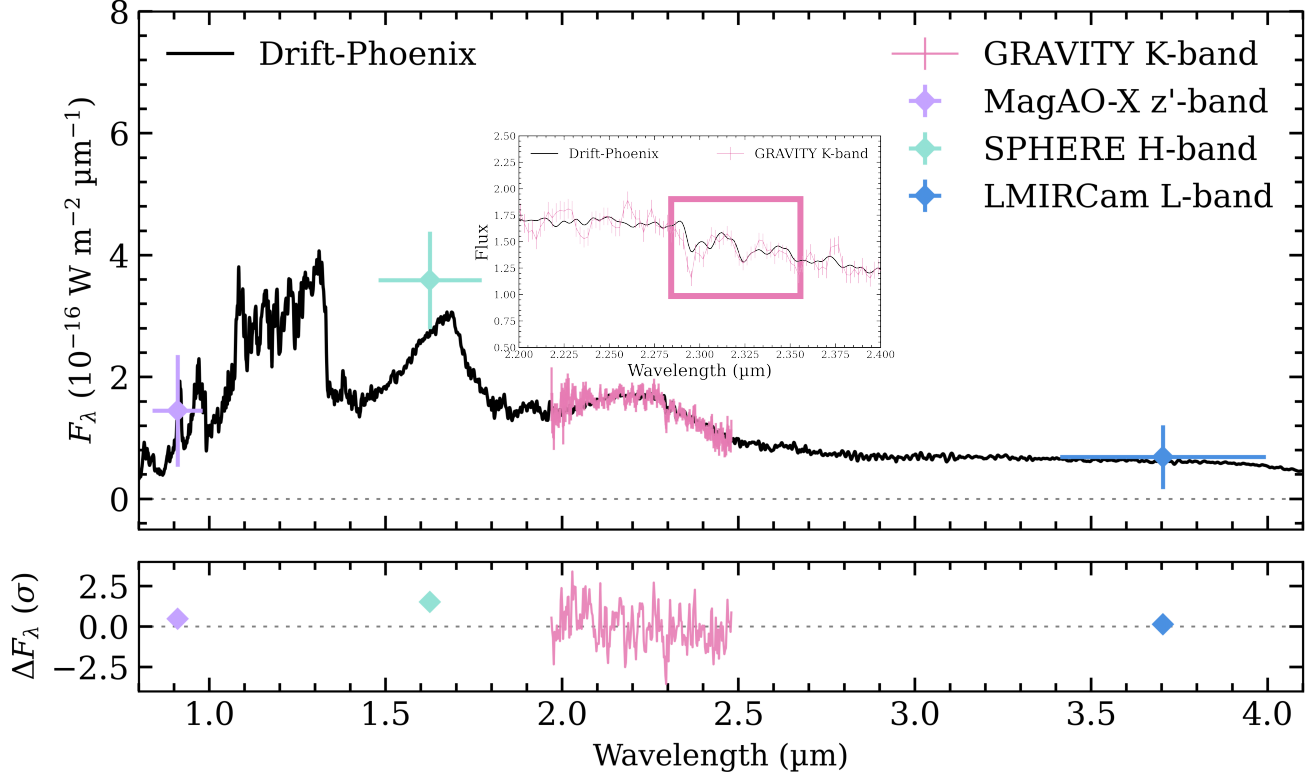


Figure 3: Drift-Phoenix spectral model overlaid with the  $K$ -band spectrum obtained with VLT/GRAVITY,  $H$ -band VLT/SPHERE,  $z'$ -band MagAO-X, and  $L$ -band LBTI/LMIRCam photometry of WISPIT 2c. The modelled spectrum is based on max likelihood fitting of temperature and radius. Figure also contains zoomed region of 2.2–2.4  $\mu\text{m}$  to highlight CO absorption band-heads, marked by the pink box.

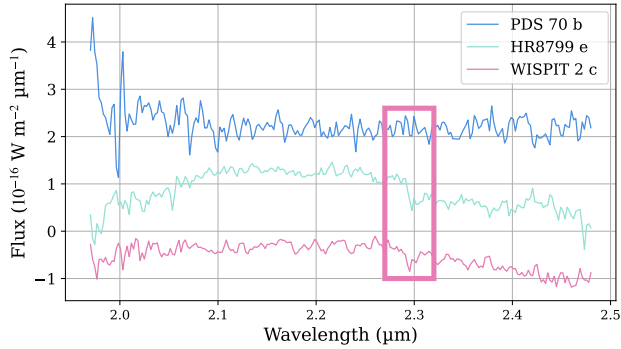


Figure 4:  $K$ -band GRAVITY spectra of PDS 70b and HR8799 e (Kammerer et al. 2025), and WISPIT 2c, offsets have been applied along the y-axis. The CO feature (highlighted by the pink box) can be clearly seen in HR8799, and WISPIT 2c, but is lacking in PDS 70b.

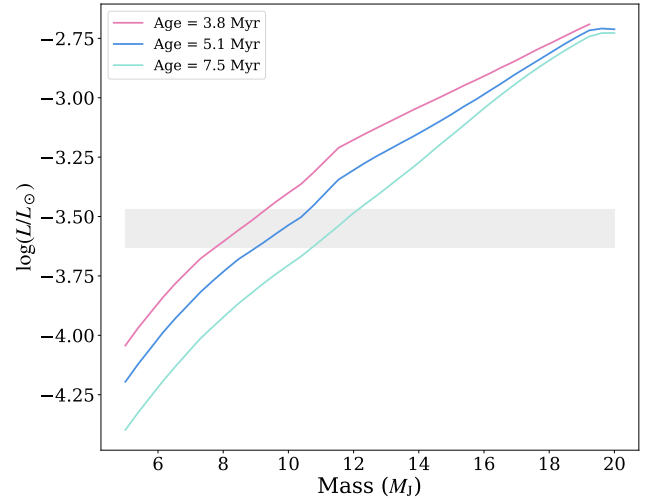
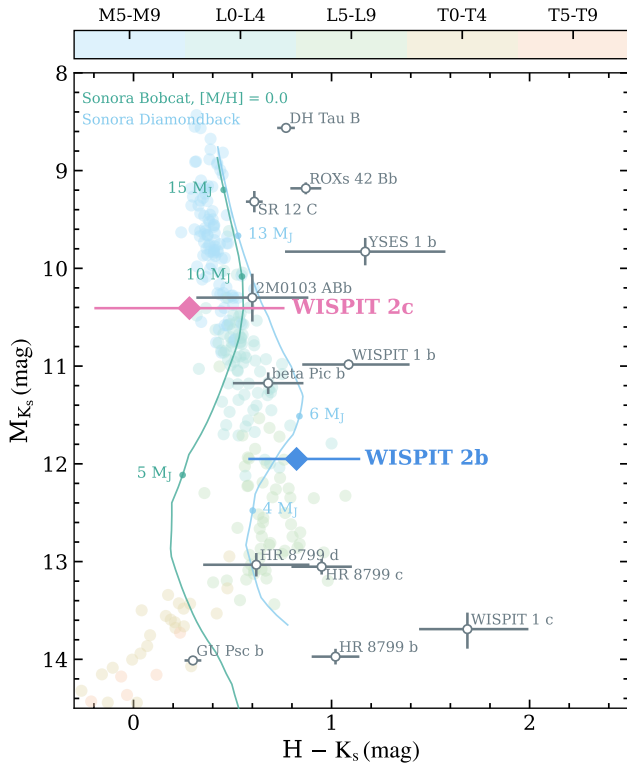


Figure 5: Sonora-Diamondback luminosity-mass isochrones at varying ages, measured luminosities from the atmospheric model fitting are shown by the grey shaded region.

627 that if a CPD is indeed present, then the dust grain  
628 sizes within the disk are on a sub-micron scale, so that



**Figure 6: Colour-magnitude diagram of the WISPIT 2 system, along with confirmed planetary companions and field brown dwarfs of various spectral types. The teal and cyan tracks show 5.1 Myr Sonora-Bobcat (cloud-free) and Sonora-Diamondback (hybrid clouds, sedimentation efficiency  $f_{\text{sed}} = 2$ ) evolutionary isochrones, respectively.**

ity for single planets is approximately 0.3, while systems with multiple planets tend to have significantly lower average eccentricities of 0.04. Similarly, Limbach & Turner (2015) reported a strong inverse correlation between planet multiplicity and orbital eccentricity. Follow-up observations will be key to constrain the orbits of both planets in the system, to establish solid links between orbital architecture and planet multiplicity.

## 5. CONCLUSIONS

Through combined photometric and spectroscopic analysis, we confirm the presence of an additional planetary mass companion in the WISPIT 2 system. The CO band-head detected in the GRAVITY  $K$ -band spectrum provides strong evidence for a planetary object, which is twice as massive as WISPIT 2b and significantly closer to the host star, with a mass range of 8-12  $M_{\text{Jup}}$  and a radial separation of 14 au. While WISPIT 2b showed strong signs of  $H\alpha$  emission, there is an absence of **significantly** detectable  $H\alpha$  emission from WISPIT 2c, which may indicate strong variability or dust veiling. With current available astrometry, the motion of the planet appears inconsistent with that of a distant background object, but further high-precision astrometric observations are needed to constrain its orbital motion. With this new detection, WISPIT 2 becomes only the second system (after PDS 70) to host multiple directly imaged young giant planets in formation, making it a prime target for follow-up observations with the upcoming ELT. This offers a rare opportunity to probe how early system architectures emerge, Although still speculative, the comparable orbital separations in both systems may hint at a “Goldilocks zone” for giant planet formation in young disks. While the available data remain limited, these results bring us one step closer to making direct connections between the initial conditions of planet formation and the final architectures of planetary systems.

The authors would like to thank an anonymous referee for comments that significantly improved the clarity of the article.

CL would like to acknowledge support from the COST Action CA22133 PLANETS.

The authors would like to thank Ilya Ilyin for fruitful discussion of their results.

We thank the Fundação para a Ciência e Tecnologia (FCT), Portugal, for the financial support to the Center for Astrophysics and Gravitation (CENTRA/IST/ULisboa) through grant No. UID/PRR/00099/2025 (<https://doi.org/10.54499/UID/PRR/00099/>

they efficiently scatter light in the optical  $z'$ -band but do not significantly contribute to the signal in the  $K$ -band. Alternatively this could indicate that there is some larger scale dusty envelope present at the position of WISPIT 2c, in fact very similar to what has been observed for PDS 70c (Stolker et al. 2020a). This envelope could then be detected in  $z'$ -band but resolved out by the interferometric GRAVITY observation. The presence of such an envelope could then also explain the non-detection at the  $H\alpha$  wavelength.

### 4.3. Planet orbital eccentricity and multiplicity

The confirmation of a second planet in the WISPIT 2 system aligns with expectations based on its dynamical behaviour. The previously detected planet in the system, WISPIT 2b, exhibits an extremely low eccentricity ( $e \leq 0.2$ ), consistent with trends observed in multi-planet systems. Studies by Xie et al. (2016) found that from a sample of *Kepler* planets, the average eccentric-

696 2025) and grant No. UID/00099/2025 ([https://doi.org/](https://doi.org/10.54499/UID/00099/2025)  
697 [10.54499/UID/00099/2025](https://doi.org/10.54499/UID/00099/2025)).

698 SFH and CS acknowledge support through UK  
699 Research and Innovation (UKRI) under the UK

700 government's Horizon Europe Funding Guarantee  
701 (EP/Z533920/1, selected in the 2023 ERC Advanced  
702 Grant round). SFH and JL acknowledge support  
703 through an STFC Small Award (ST/Y001656/1).

## REFERENCES

- 704 Allard, F. 2014, in IAU Symposium, Vol. 299, Exploring  
705 the Formation and Evolution of Planetary Systems, ed.  
706 M. Booth, B. C. Matthews, & J. R. Graham, 271–272  
707 Allard, F., Homeier, D., & Freytag, B. 2012, Philosophical  
708 Transactions of the Royal Society of London Series A,  
709 370, 2765  
710 Allers, K. N., & Liu, M. C. 2013, ApJ, 772, 79  
711 Andrews, S. M., Huang, J., Pérez, L. M., et al. 2018, ApJL,  
712 869, L41  
713 Avenhaus, H., Quanz, S. P., Garufi, A., et al. 2018, ApJ,  
714 863, 44  
715 Baron, E., Hauschildt, P. H., Allard, F., et al. 2003, in IAU  
716 Symposium, Vol. 210, Modelling of Stellar Atmospheres,  
717 ed. N. Piskunov, W. W. Weiss, & D. F. Gray, 19  
718 Baudino, J.-L., Bézar, B., Boccaletti, A., et al. 2015,  
719 A&A, 582, A83  
720 Beuzit, J.-L., Vigan, A., Mouillet, D., et al. 2019, A&A,  
721 631, A155  
722 Blunt, S., Wang, J. J., Angelo, I., et al. 2020, AJ, 159, 89  
723 Boss, A. P. 1997, Science, 276, 1836  
724 Bourdarot, G., Eisenhauer, F., Yazıcı, S., et al. 2024, arXiv  
725 e-prints, arXiv:2409.08438  
726 Cesetti, M., Pizzella, A., Ivanov, V. D., et al. 2013, A&A,  
727 549, A129  
728 Charnay, B., Bézar, B., Baudino, J.-L., et al. 2018, ApJ,  
729 854, 172  
730 Close, L. M., van Capelleveen, R. F., Weible, G., et al.  
731 2025a, ApJL, 990, L9  
732 Close, L. M., Males, J. R., Li, J., et al. 2025b, AJ, 169, 35  
733 Currie, T., Biller, B., Lagrange, A., et al. 2023, in  
734 Astronomical Society of the Pacific Conference Series,  
735 Vol. 534, Protostars and Planets VII, ed. S. Inutsuka,  
736 Y. Aikawa, T. Muto, K. Tomida, & M. Tamura, 799  
737 Currie, T., Lawson, K., Schneider, G., et al. 2022, Nature  
738 Astronomy, 6, 751  
739 Cutri, R. M., Skrutskie, M. F., van Dyk, S., et al. 2003,  
740 2MASS All Sky Catalog of point sources.  
741 Dohlen, K., Langlois, M., Saisse, M., et al. 2008, in Society  
742 of Photo-Optical Instrumentation Engineers (SPIE)  
743 Conference Series, Vol. 7014, Ground-based and Airborne  
744 Instrumentation for Astronomy II, ed. I. S. McLean &  
745 M. M. Casali, 70143L  
746 Dong, R., Hashimoto, J., Rafikov, R., et al. 2012, ApJ, 760,  
747 111  
748 Ercolano, B., Mayr, D., Owen, J. E., Rosotti, G., &  
749 Manara, C. F. 2014, MNRAS, 439, 256  
750 Flock, M., Nelson, R. P., Turner, N. J., et al. 2017, ApJ,  
751 850, 131  
752 Foreman-Mackey, D., Conley, A., Meierjürgen Farr, W.,  
753 et al. 2013, emcee: The MCMC Hammer, Astrophysics  
754 Source Code Library, record ascl:1303.002, , ,  
755 ascl:1303.002  
756 Gaia Collaboration, Vallenari, A., Brown, A. G. A., et al.  
757 2023, A&A, 674, A1  
758 Garufi, A., Ginski, C., van Holstein, R. G., et al. 2024,  
759 A&A, 685, A53  
760 Ginski, C., Garufi, A., Benisty, M., et al. 2024, A&A, 685,  
761 A52  
762 GRAVITY+ Collaboration. 2025, arXiv e-prints,  
763 arXiv:2509.21431  
764 GRAVITY Collaboration, Abuter, R., Accardo, M., et al.  
765 2017a, A&A, 602, A94  
766 —. 2017b, A&A, 602, A94  
767 GRAVITY Collaboration, Lacour, S., Nowak, M., et al.  
768 2019, A&A, 623, L11  
769 Gregorio-Hetem, J., Lepine, J. R. D., Quast, G. R., Torres,  
770 C. A. O., & de La Reza, R. 1992, AJ, 103, 549  
771 Haffert, S. Y., Bohn, A. J., de Boer, J., et al. 2019, Nature  
772 Astronomy, 3, 749  
773 Hammond, I., Christiaens, V., Price, D. J., et al. 2023,  
774 MNRAS, 522, L51  
775 Hashimoto, J., Dong, R., Kudo, T., et al. 2012, ApJL, 758,  
776 L19  
777 Hashimoto, J., Tsukagoshi, T., Brown, J. M., et al. 2015,  
778 ApJ, 799, 43  
779 Hauschildt, P. H., & Baron, E. 1999, Journal of  
780 Computational and Applied Mathematics, 109, 41  
781 Helling, C., Dehn, M., Woitke, P., & Hauschildt, P. H.  
782 2008a, ApJL, 675, L105  
783 Helling, C., & Woitke, P. 2006, A&A, 455, 325  
784 Helling, C., Woitke, P., & Thi, W.-F. 2008b, A&A, 485, 547  
785 Kammerer, J., Winterhalder, T. O., Lacour, S., et al. 2025,  
786 A&A, 704, A318  
787 Keppler, M., Benisty, M., Müller, A., et al. 2018, A&A,  
788 617, A44

- 789 Kepler, M., Teague, R., Bae, J., et al. 2019, *A&A*, 625,  
790 A118
- 791 Kurtovic, N. T., Pérez, L. M., Benisty, M., et al. 2018,  
792 *ApJL*, 869, L44
- 793 Kuznetsova, A., Bae, J., Hartmann, L., & Mac Low, M.-M.  
794 2022, *ApJ*, 928, 92
- 795 Lapeyrere, V., Kervella, P., Lacour, S., et al. 2014, in  
796 Society of Photo-Optical Instrumentation Engineers  
797 (SPIE) Conference Series, Vol. 9146, Optical and Infrared  
798 Interferometry IV, ed. J. K. Rajagopal, M. J.  
799 Creech-Eakman, & F. Malbet, 91462D
- 800 Limbach, M. A., & Turner, E. L. 2015, Proceedings of the  
801 National Academy of Sciences, 112, 20.  
802 <https://www.pnas.org/doi/abs/10.1073/pnas.1406545111>
- 803 Lissauer, J. J., Batalha, N. M., & Borucki, W. J. 2023, in  
804 Astronomical Society of the Pacific Conference Series,  
805 Vol. 534, Protostars and Planets VII, ed. S. Inutsuka,  
806 Y. Aikawa, T. Muto, K. Tomida, & M. Tamura, 839
- 807 MacKay, D. J. C. 2003, *Information Theory, Inference, and*  
808 *Learning Algorithms* (Copyright Cambridge University  
809 Press)
- 810 Manara, C. F., Ansdell, M., Rosotti, G. P., et al. 2023, in  
811 Astronomical Society of the Pacific Conference Series,  
812 Vol. 534, Protostars and Planets VII, ed. S. Inutsuka,  
813 Y. Aikawa, T. Muto, K. Tomida, & M. Tamura, 539
- 814 Manara, C. F., Frasca, A., Venuti, L., et al. 2021, *A&A*,  
815 650, A196
- 816 Marcus, P. S., Pei, S., Jiang, C.-H., et al. 2015, *ApJ*, 808, 87
- 817 Marley, M. S., & Sengupta, S. 2011, *MNRAS*, 417, 2874
- 818 Marley, M. S., Saumon, D., Visscher, C., et al. 2021, *ApJ*,  
819 920, 85
- 820 Marois, C., Macintosh, B., Barman, T., et al. 2008, *Science*,  
821 322, 1348
- 822 Milli, J., Mouillet, D., Lagrange, A.-M., et al. 2012, *A&A*,  
823 545, A111
- 824 Morley, C. V., Mukherjee, S., Marley, M. S., et al. 2024,  
825 *ApJ*, 975, 59
- 826 Nasedkin, E., Mollière, P., Lacour, S., et al. 2024, *A&A*,  
827 687, A298
- 828 Nowak, M., Lacour, S., Lagrange, A.-M., et al. 2020, *A&A*,  
829 642, L2
- 830 Öberg, K. I., Guzmán, V. V., Walsh, C., et al. 2021, *ApJS*,  
831 257, 1
- 832 Patience, J., King, R. R., De Rosa, R. J., et al. 2012, *A&A*,  
833 540, A85
- 834 Perotti, G., Christiaens, V., Henning, T., et al. 2023,  
835 *Nature*, 620, 516
- 836 Phillips, M. W., Tremblin, P., Baraffe, I., et al. 2020, *A&A*,  
837 637, A38
- 838 Pollack, J. B., Hubickyj, O., Bodenheimer, P., et al. 1996,  
839 *Icarus*, 124, 62
- 840 Rajpurohit, A. S., Reylé, C., Schultheis, M., et al. 2012,  
841 *A&A*, 545, A85
- 842 Rukdee, S. 2024, *Scientific Reports*, 14, 27356
- 843 Schneider, J., Dedieu, C., Le Sidaner, P., Savalle, R., &  
844 Zolotukhin, I. 2011, *A&A*, 532, A79
- 845 Speagle, J. S. 2020, *MNRAS*, 493, 3132
- 846 Spiegel, D. S., & Burrows, A. 2012, *ApJ*, 745, 174
- 847 Stolker, T., Marleau, G.-D., Cugno, G., et al. 2020a, *A&A*,  
848 644, A13
- 849 Stolker, T., Quanz, S. P., Todorov, K. O., et al. 2020b,  
850 *A&A*, 635, A182
- 851 Suriano, S. S., Li, Z.-Y., Krasnopolsky, R., & Shang, H.  
852 2018, *MNRAS*, 477, 1239
- 853 Trevascus, D., Blunt, S., Christiaens, V., et al. 2025, *A&A*,  
854 698, A19
- 855 van Capelleveen, R. F., Ginski, C., Kenworthy, M. A., et al.  
856 2025, *ApJL*, 990, L8
- 857 Wang, J. J., Vigan, A., Lacour, S., et al. 2021, *AJ*, 161, 148
- 858 Witte, S., Helling, C., Barman, T., Heidrich, N., &  
859 Hauschildt, P. H. 2011, *A&A*, 529, A44
- 860 Witte, S., Helling, C., & Hauschildt, P. H. 2009, *A&A*, 506,  
861 1367
- 862 Woitke, P., & Helling, C. 2003, *A&A*, 399, 297  
863 —. 2004, *A&A*, 414, 335
- 864 Xie, J.-W., Dong, S., Zhu, Z., et al. 2016, Proceedings of  
865 the National Academy of Science, 113, 11431
- 866 Zhou, Y., Bowler, B. P., Sanghi, A., et al. 2025, *ApJL*, 980,  
867 L39

## APPENDIX

## A. FLUX CALIBRATION OF THE GRAVITY DATA

868  
869  
870 The SED from the star was obtained by fitting the photometry point from GAIA DR3 (Gaia Collaboration et al.  
871 2023) and 2MASS (Cutri et al. 2003), used in van Capelleveen et al. (2025). The absolute flux of the star was obtained  
872 with a synthetic spectrum from the `species`<sup>3</sup> package, using a BT-Settl-CIFIST stellar model. The result of the fit of  
873 the SED is shown in Fig. 7. Finally, the absolute flux of the planet spectrum is obtained by multiplying the contrast  
874 spectrum extracted from the `exogravity` pipeline with the synthetic spectrum of the star.

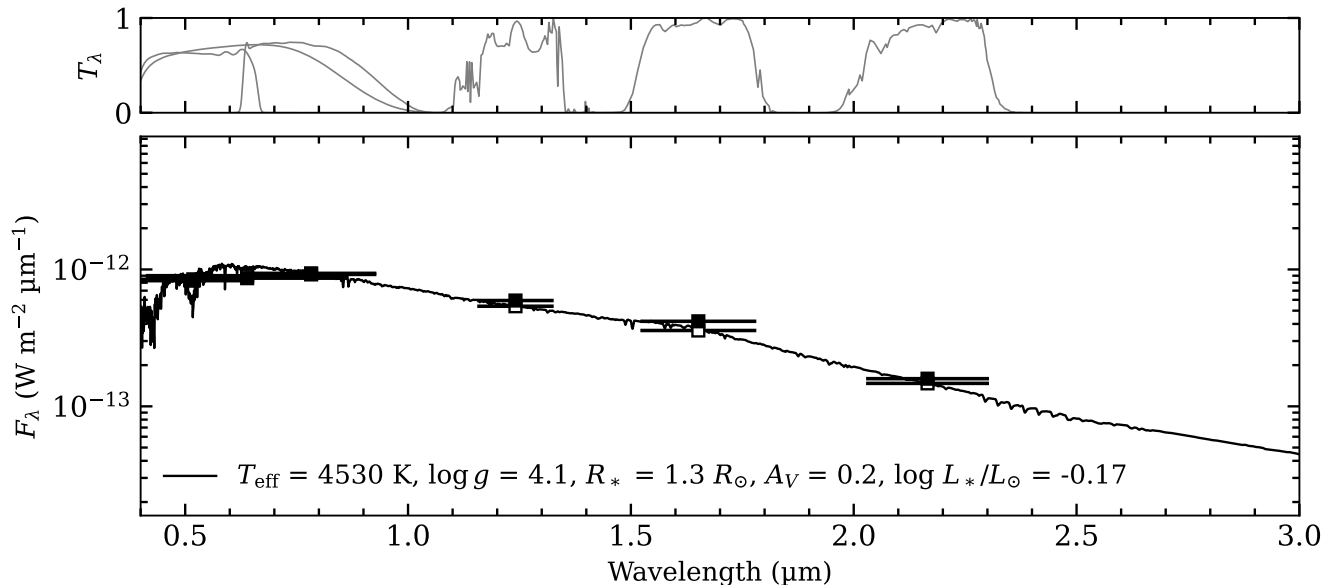


Figure 7: Stellar SED of WISPIT 2 fitted used for the absolute flux calibration of the GRAVITY data.

## B. COMPARISON OF THE TWO SPHERE OBSERVATION EPOCHS

875  
876 We show the RDI reduced (total intensity) SPHERE observations taken in March and September  
877 2025 in Fig. 8. Both were taken with similar instrument settings and in the  $H$ -band filter. The main  
878 difference between the two epochs is the applied reference star data. While for the September 2025  
879 epoch a dedicated reference star was observed in “star-hopping mode”, i.e. interleaved with the science  
880 observation, this was not the case for the March 2025 data. For this data set instead a reference library  
881 was utilised. Both observation epochs recover the companion at high significance.

## C. RGB IMAGE OF THE WISPIT 2 SYSTEM

882  
883 In Fig. 9 we show an RGB image of the WISPIT 2 system using existing literature data as well as our new SPHERE  
884  $H$ -band observations. The red channel in the image is comprised of the ADI treated  $L$ -band data from Close et al.  
885 (2025a), while the green channel uses the RDI treated SPHERE  $K$ -band data first presented in van Capelleveen et al.  
886 (2025). The blue channel uses our newly obtained SPHERE  $H$ -band data. Here we use itself a composite of the RDI  
887 treated annulus confined data that recovers the planet WISPIT 2c and which is shown in Fig. 1, and a polarisation  
888 image showing the disk scattered light created from the same data set (but not sensitive to the planet). Each channel  
889 was normalised such that the disk has a similar brightness towards its forward scattering peak. The brightness of each

<sup>3</sup> <https://species.readthedocs.io/>

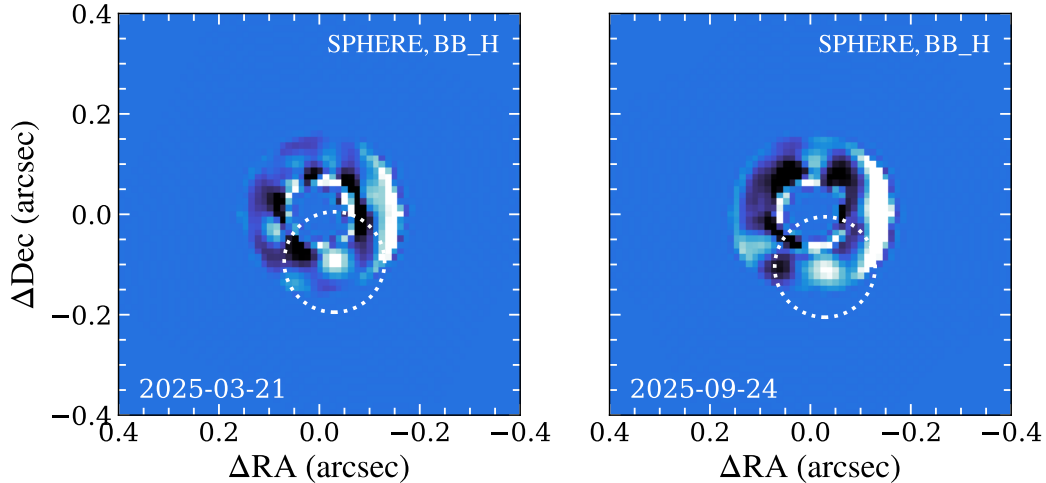


Figure 8: SPHERE  $H$ -band observations of the new planet WISPIT 2c. Both observation epochs clearly recover the planet (marked with the dotted circle). A mask is applied to exclude the majority of disk signal from the extraction and prevent over-subtraction. Both images utilise a linear colour map.

channel is scaled with the square root of the pixel values, which provides good contrast between planet signal and noise. We note that this image should be primarily considered for illustration of the system architecture and is not meant for an accurate colour analysis of the disk or the planet signal.

#### D. FULL NESTED SAMPLING INFERENCE OF PLANET ATMOSPHERE PARAMETERS

We performed a full atmospheric **parameter inference** of WISPIT 2c using the `species` tool (Stolker et al. 2020b). The **analysis** combines both the medium resolution  $K$ -band spectrum extracted from the GRAVITY observations, using the standard deviation errors of the spectrum, and the  $z'$ -,  $H$ - and  $L$ -band photometry.

We use the Drift-Phoenix (Hauschildt & Baron 1999; Baron et al. 2003; Woitke & Helling 2003, 2004; Helling & Woitke 2006; Helling et al. 2008a,b; Witte et al. 2009, 2011), Sonora-Diamondback (Morley et al. 2024), ExoRem (Baudino et al. 2015; Charnay et al. 2018), BT-Dusty (Allard et al. 2012), Sonora-Bobcat (Marley et al. 2021), BT-Settl (Allard 2014), and ATMO (Phillips et al. 2020) models to explore a variety of physical properties for the planetary atmosphere. The model grids cover a wavelength range of 0.5-10  $\mu\text{m}$  with a spectral resolution of 500 (consistent with that of the GRAVITY instrument) and 1000 live points. We adopted uniform priors with reasonable ranges of 1500 - 3000 K and 0.5 - 3.5  $R_J$ . We fix the surface gravity  $\log g$  at 3.9 for all models (average of reported values for young gas giants), with the exception BT-Dusty, where it was fixed at 4.5, as this is the minimum value accepted by the model grid.

We do not attempt to **constrain** these values as the continuum shape is only marginally influenced by  $\log g$  and we do not resolve any individual spectral lines that would be strongly influenced (see Fig. 10). Because the GRAVITY spectrum has a moderate spectral resolution, the  $K$ -band spectrum is not sensitive enough to the depth of lines to determine the abundances of individual elements (Rukdee 2024) (see Fig. 11). For this reason we fix the metallicity at 0.0, assuming a solar value. The resulting posterior distributions for **our best fit Drift-Phoenix model** are shown in Fig. 12. Additional analysis determined that the **atmospheric constraints** are dominated by the  $K$ -band spectrum. Starting from the  $K$ -band spectrum we ran our sampler to extract the planet parameters and adding  $L$ -,  $H$ -, and  $z'$  in that order. We find this produces only a very minimal change in temperature, on the order of tens of kelvin, letting us include all photometric points in the final fits. We show in Fig. 13, a **comparison of our test models**. As the fits with the smallest residuals appear to be Drift-Phoenix and ExoRem, this may imply a **cloudy atmosphere**. Although we do note that both BT-Settl and Sonora-Diamondback also employ cloud physics but are not ideal fits to the data.

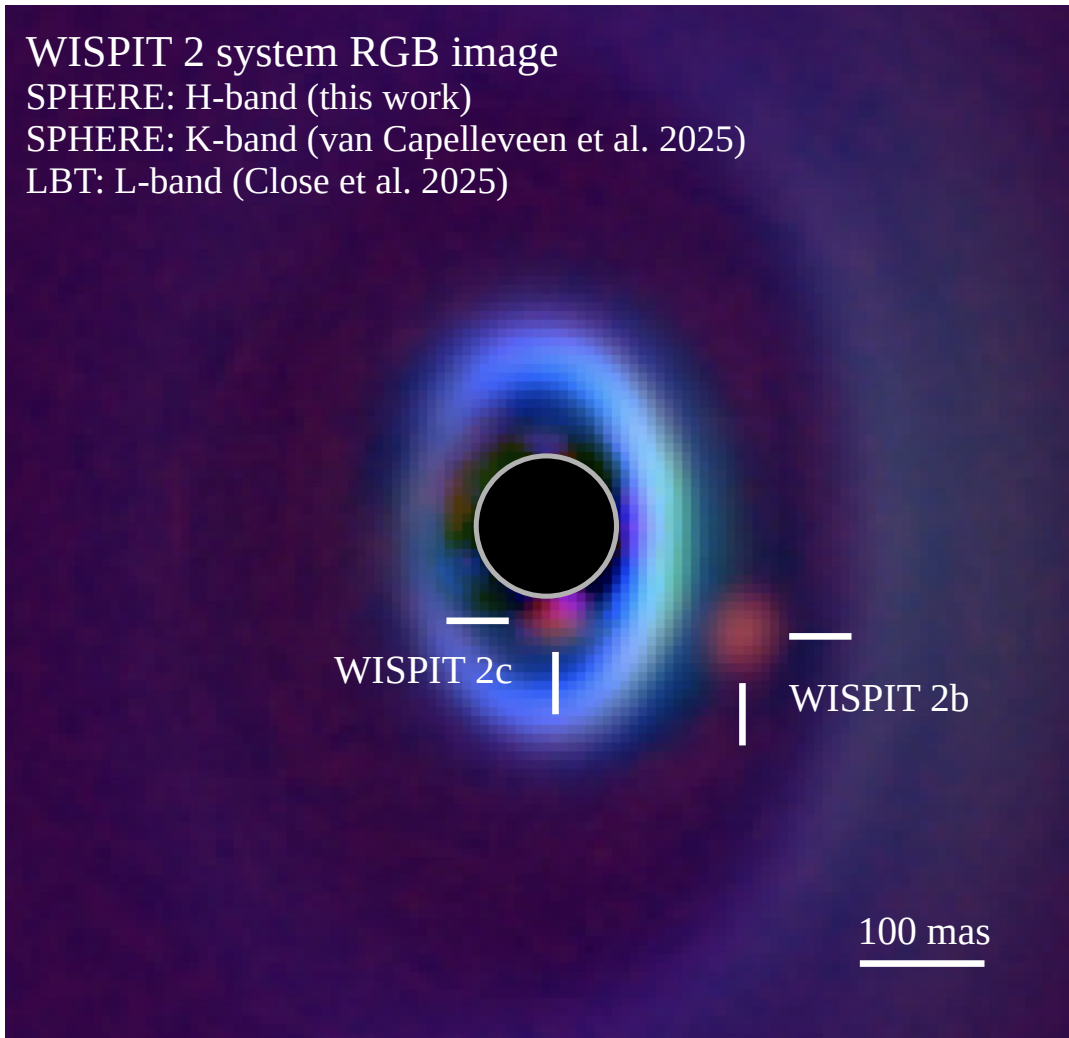


**Figure 9:** RGB image of WISPIT 2 using the existing  $L$ - and  $K$ -band data by [Close et al. \(2025a\)](#) and [van Capelleveen et al. \(2025\)](#), as well as our new  $H$ -band data. We mark the positions of the known planet WISPIT 2b as well as the new inner planet WISPIT 2c.

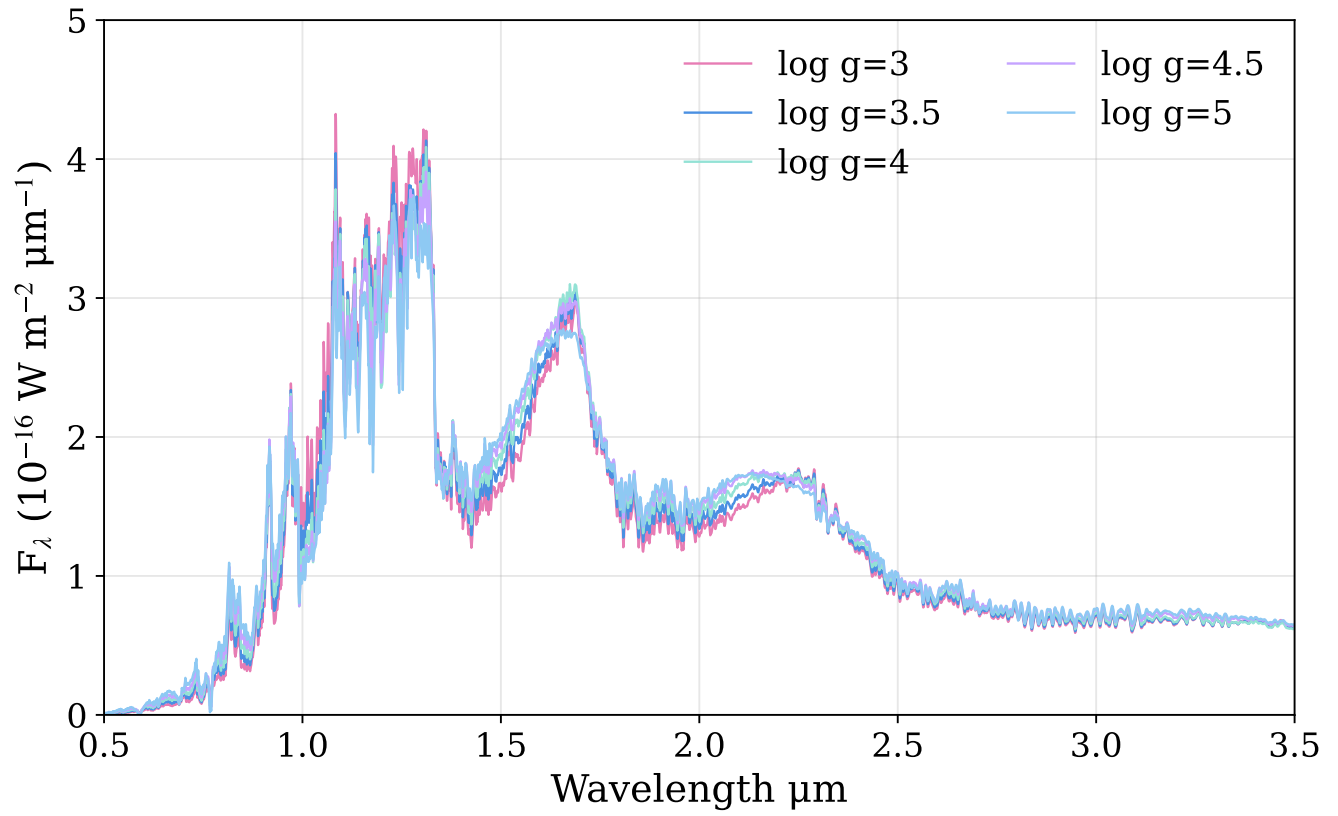


Figure 10: Drift-Phoenix model spectrum of the WISPIT 2c atmosphere with varying  $\log g$ , at a fixed temperature of 1750 K and a radius of  $1.78 R_{\text{Jup}}$ .

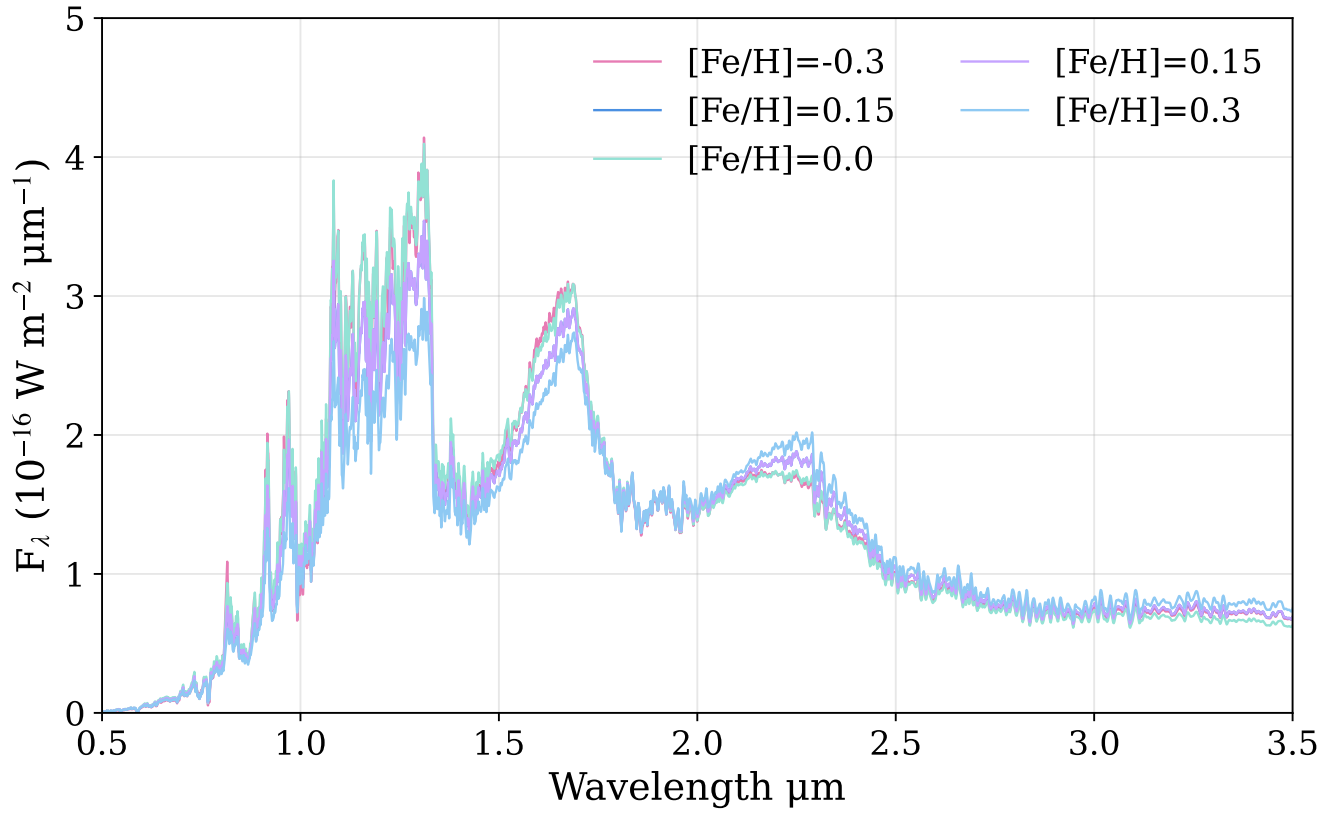


Figure 11: Drift-Phoenix model spectrum of the WISPIT 2c atmosphere with varying metallicity, at a fixed temperature of 1750 K and a radius of 1.78  $R_{\text{Jup}}$ .

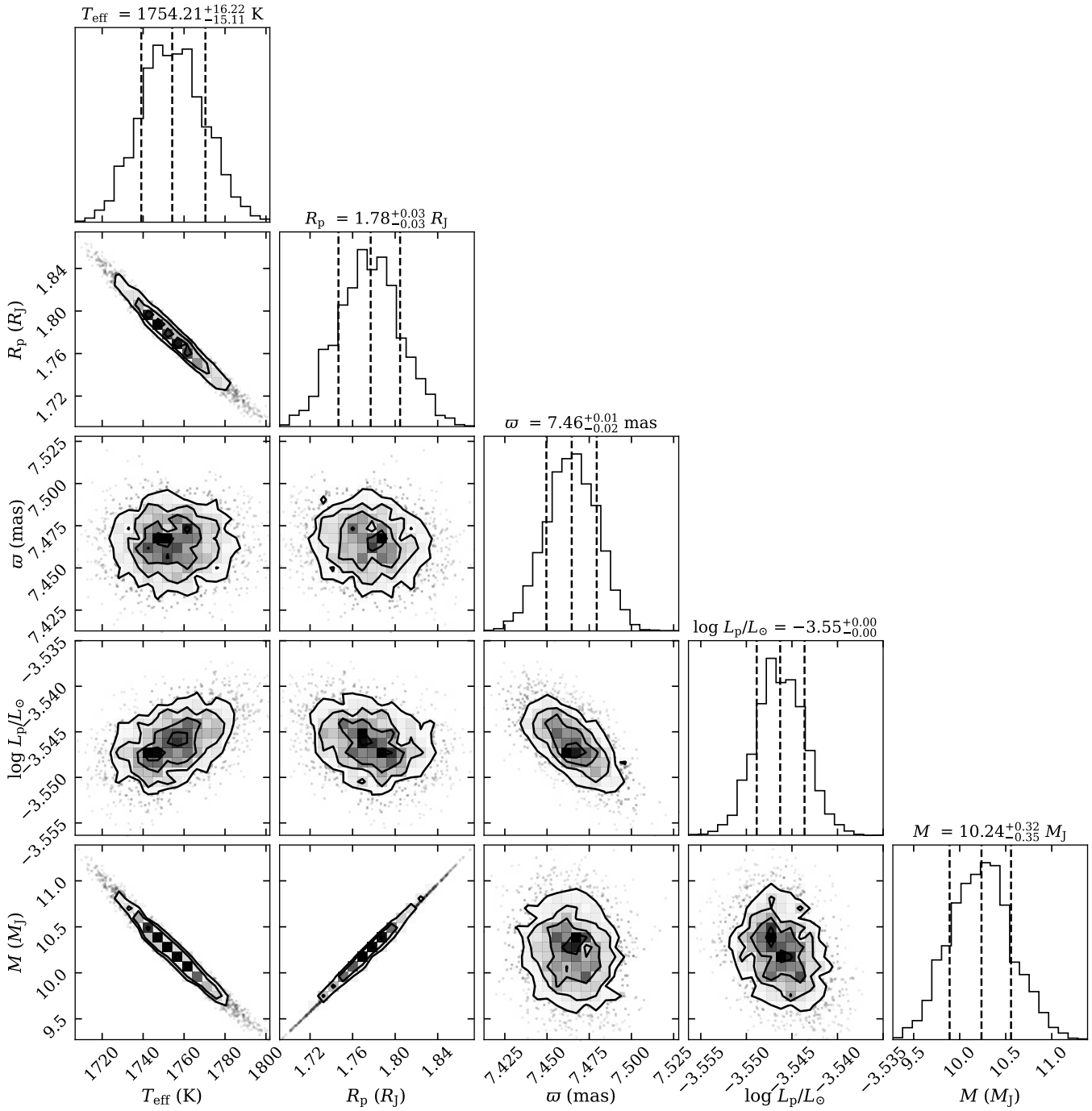
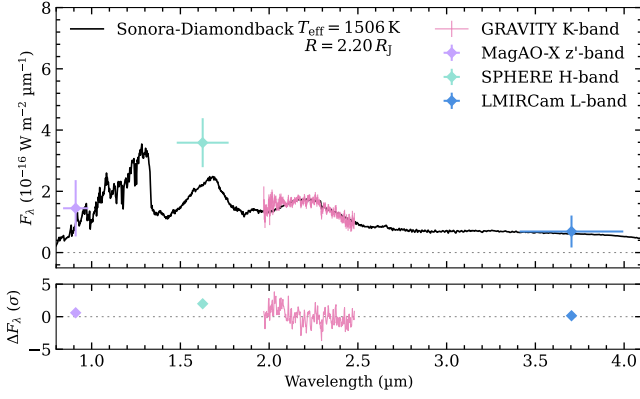
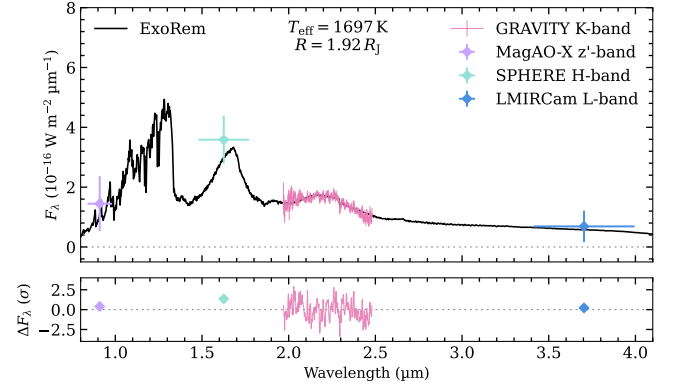


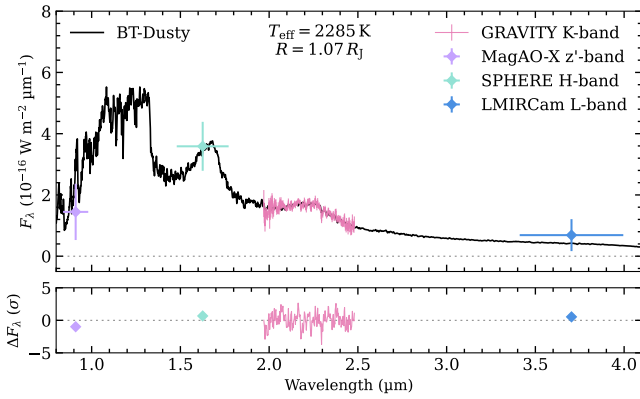
Figure 12: Posterior distributions for WISPIT 2c from the nested-sampling using Drift-Phoenix, with median values shown and  $\pm 1\sigma$ .



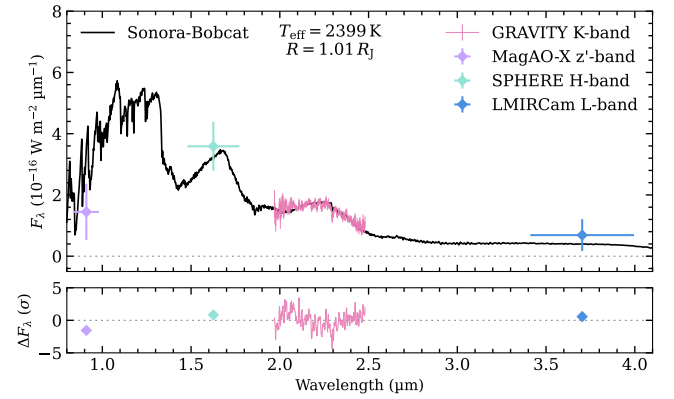
(a) Sonora-Diamondback best fit spectrum with inferred planet temperature and radius.



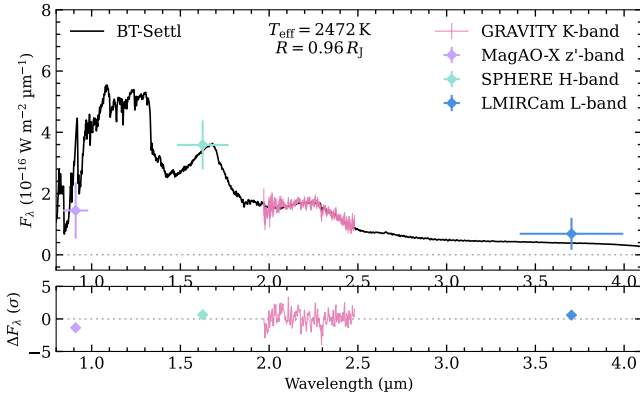
(b) ExoRem best fit spectrum with inferred planet temperature and radius.



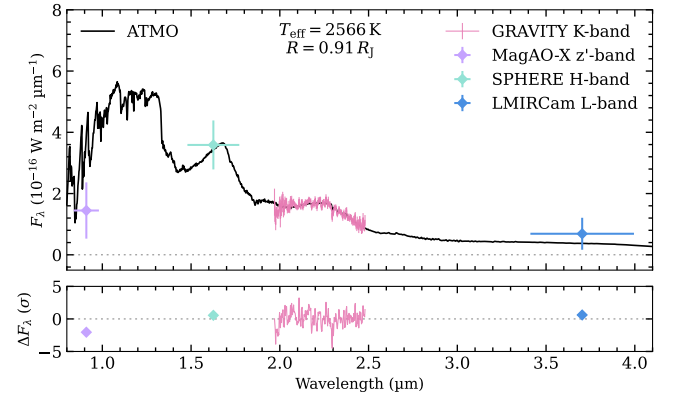
(c) BT-Dusty best fit spectrum with inferred planet temperature and radius.



(d) Sonora-Bobcat best fit spectrum with inferred planet temperature and radius.



(e) BT-Settl best fit spectrum with inferred planet temperature and radius.



(f) ATMO best fit spectrum with inferred planet temperature and radius.

Figure 13: Exploration of multiple model grids.